

Urban atmospheric boundary-layer structure in complex topography: an empirical 3D case study for Stuttgart, Germany

Matthias Zeeman, Christopher Claus Holst, Meinolf Kossmann, Daniel Leukauf, Christoph Münkkel, Andreas Philipp, Rayk Rinke, Stefan Emeis

Angaben zur Veröffentlichung / Publication details:

Zeeman, Matthias, Christopher Claus Holst, Meinolf Kossmann, Daniel Leukauf, Christoph Münkkel, Andreas Philipp, Rayk Rinke, and Stefan Emeis. 2022. "Urban atmospheric boundary-layer structure in complex topography: an empirical 3D case study for Stuttgart, Germany." *Frontiers in Earth Science* 10 (March): 840112.
<https://doi.org/10.3389/feart.2022.840112>.

Supplementary Material

1 MATERIAL AND METHODS

1.1 Comparison of Doppler lidar and radio sounding profiles

The nearby radio sounding station Schnarrenberg is located approximately 6 km north of the Stuttgart City centre. However, a comparison of Doppler lidar (DL) wind profile data with radio sounding (RS) data showed that a relevant portion of the atmospheric boundary layer (ABL) up to an altitude of 1000 m a.s.l., or 750 m depth, is captured by the DL setup (Figure S2 and Figure S3). The influence of local topography is shown closer to the surface, e.g., the proximity of the Neckar river valley to the RS station. Hence these lower altitude RS statistics differ substantially from the DL at a similar altitude.

1.2 Backscatter profiles

The determination of backscatter profiles followed different routines for the DL and ceilometer (CL) systems, hence we considered a comparison to be useful for cross-validation. First, the CL and DL systems record backscatter information at different wavelengths. Second, the DL profiles were not determined from vertical stare observations as the CL profiles, but instead were derived at the intercept of three concerted DL beams at a minimum of 500 m from the nearest DL unit. Therefore, the observations near roof level were not limited by poor signal quality in the nearest DL range gates. The outcomes show, however, that the DL cannot replace the CL as the backscatter signals differ substantially (Figure S4). First, clouds and cloud layers are detected by both systems, but where precipitation is apparent in the CL data, the DL observations did not highlight these clearly in the backscatter signal (Figure S4). Second, the DL and CL showed similar short-term variability in the backscatter signal of cloud layers (Figure S4 panel A and C; e.g., shortly before sunrise), meaning these perturbations are evidence of real variability in cloud base properties and may provide opportunities for further study, e.g., on entrainment processes. Third, both CL and DL helped identify layers below 500 m depth. The CL data revealed gradients in backscatter signal below a depth of 300 m that are not clearly visible in the DL backscatter information (Figure S4). By design, a lidar telescope performance varies with range distances. Different retrieval algorithms may be used for sections of the resolved range and we assume here that some artifacts are present in gradients below 300 m depth. Such retrieval artifacts may be introduced by incomplete overlap in the bi-axial design. However, there is enough evidence from the wind field data to support that identified layers below 300 m depth existed and reoccurred frequently, hence the CL retrievals at low altitude cannot be dismissed.

1.3 Model simulation

We used the Weather Research and Forecasting (WRF) Model v3.8.1, a non-hydrostatic, fully compressible model that uses a staggered Arakawa-C grid and a terrain-following pressure vertical coordinate (Daniels et al., 2016). The model set-up is similar to Talbot et al. (2012), who used six model domains nested sequentially where the outer three model nests are run in URANS mode and the three innermost domains are run in LES mode. The sixth model domain has been removed to limit computational costs. Vertical grid stretching was applied. The outermost domain has a resolution of 12150 m, from which the mesh size was decreased step-wise by a factor 3 to approach 150 m for the innermost domain. The lowest model level lies at 10 m above ground and the vertical mesh size was 15 m near the surface and increases with height. The innermost domain has a size of $300 \times 300 \times 79$ data points.

The horizontal resolution of this setup does not allow for a full development of turbulence structures, and it is not the goal of this simulation to resolve these. The resolution is however fine enough to resolve the terrain and its effect on the mean flow.

1.3.1 Model parameters

The YSU PBL scheme (Hong et al., 2006) was applied for the three outer, mesoscale domains and horizontal diffusion is parameterized using 2D deformation in these domains. The LES domains are run without a PBL scheme and the 1.5 order three-dimensional turbulence kinetic energy (TKE) closure (Deardorff, 1980) is applied for diffusion. Surface layer processes are parameterized using the revised MM5 surface layer scheme (Jiménez et al., 2011). Other physics parametrizations include the rapid radiative transfer model (Mlawer et al., 1997) for long wave radiation and the Dhudia scheme (Dudhia, 1988) for short wave radiation, the WRF single moment three class scheme (Hong et al., 2004) and the NOAH land surface model (Niu et al., 2011) with four soil layers. The integration in time is done with a 3rd order Runge-Kutta scheme. Horizontal (vertical) advection is calculated with a 5th (3rd) order scheme. Time steps of 60, 20, 5, 1, 0.25 s were used in domain 1, 2, 3, 4, 5, respectively.

1.3.2 Model topography

Data sources for topography and land use for the coarse domains were the global 30 arc-second elevation (GTOPO30) and the US Geological Survey (USGS) land use data sets. For the LES domains, the ASTER topography data set (Schmugge et al., 2003) and the CORINE Land use data set CLC12 were used. A redefinition of CORINE land use categories to the 24 USGS categories was done following Pineda et al. (2004). The initial- and boundary conditions were taken from the ECMWF operational analysis at 6 hour interval. The simulations were initialized on the 13 Feb 2017, 00:00 UTC and ran for 54 hours. The first 24 hours were considered as model spin-up and were not analysed.

2 SUPPLEMENTARY TABLES AND FIGURES

2.1 Figures



Figure S1. The situation of Stuttgart, Germany, within central Europe, indicating main administrative borders, lakes and rivers. The inset corresponds the area shown in Figure 1B.

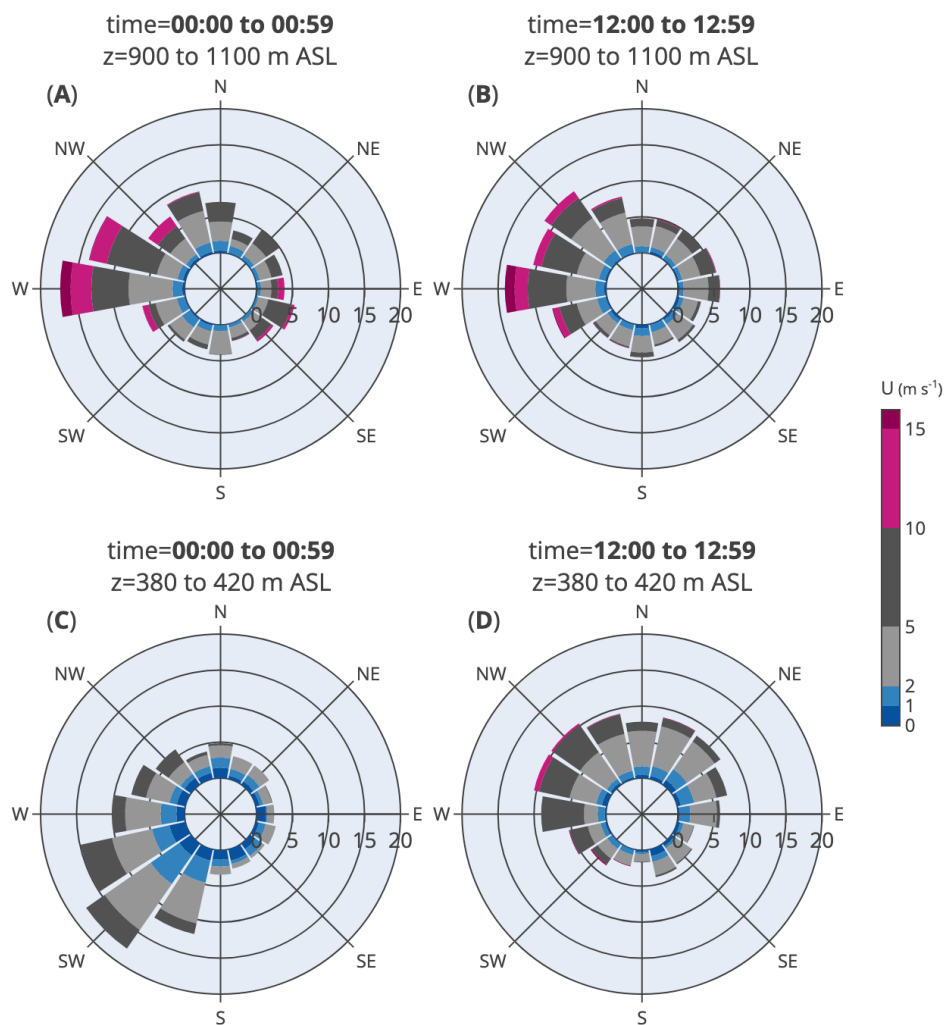


Figure S2. Wind distributions for Doppler lidar (DL) profiles in Stuttgart for 00 UTC (left) and 12 UTC (right) for two altitude (z) ranges (top, bottom), between 15 Mar 2017 and 30 Jun 2017.

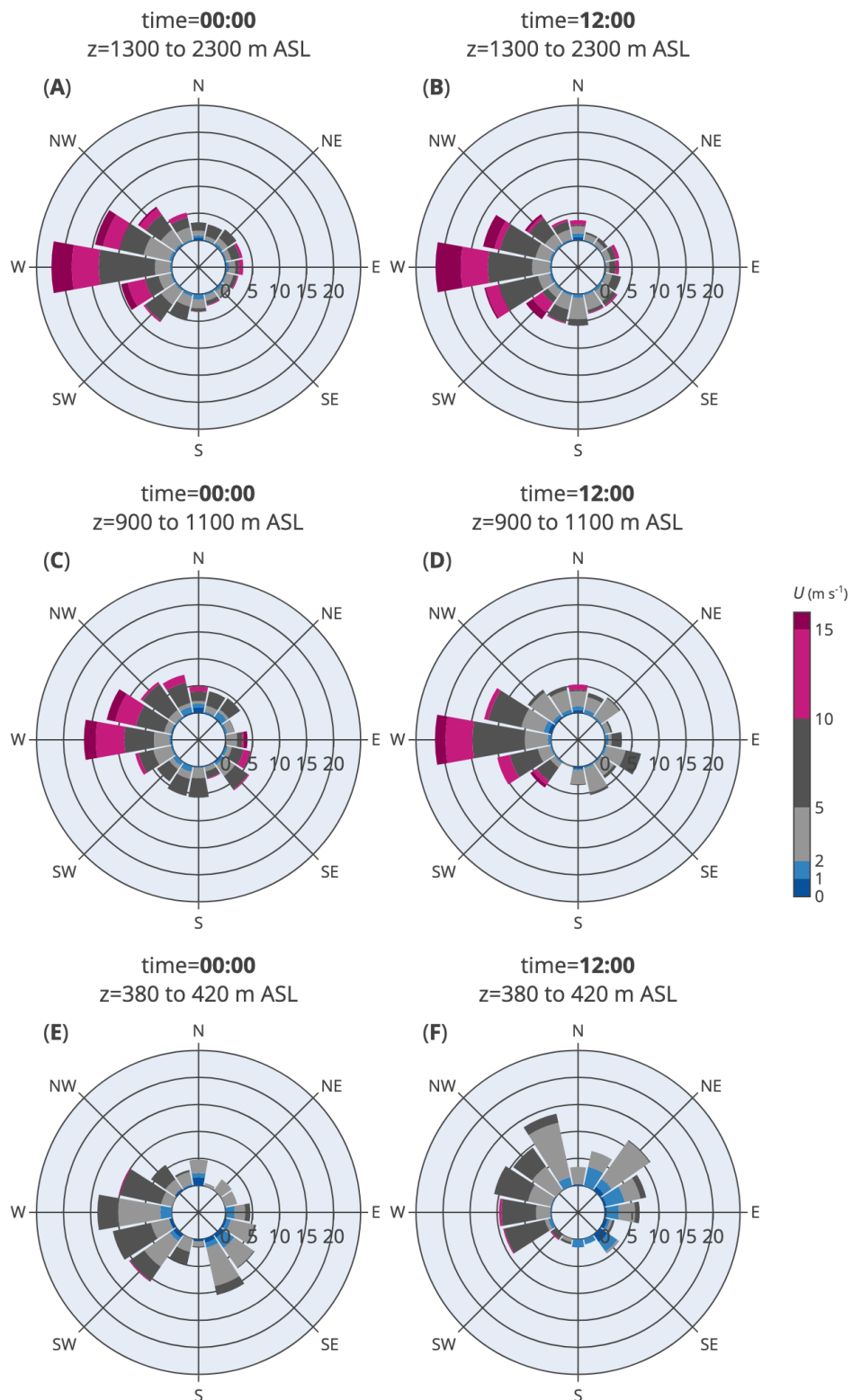


Figure S3. Wind distributions for radio soundings from Stuttgart Schnarrenberg for 00 UTC (left) and 12 UTC (right) for three altitude (z) ranges (top, centre, bottom), between 15 Mar 2017 and 30 Jun 2017. Data provided by the German Weather Service (DWD).

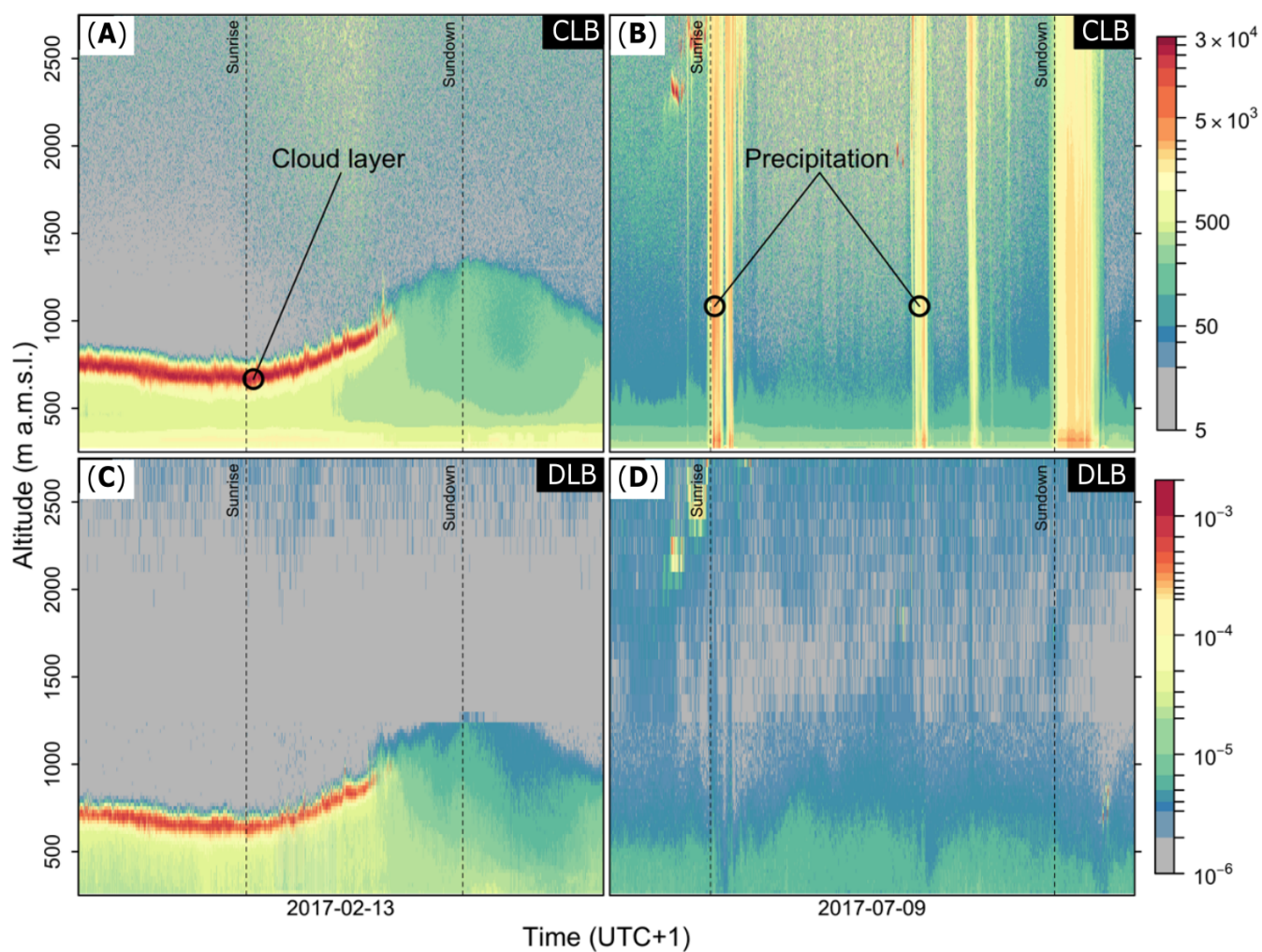


Figure S4. The ceilometer backscatter (CLB) and Doppler lidar backscatter (DLB) signals are shown in the top and bottom panels, respectively, for selected days (00:00 to 23:59) in winter (left) and summer (right). Sunrise and sunset are indicated by dashed vertical lines.

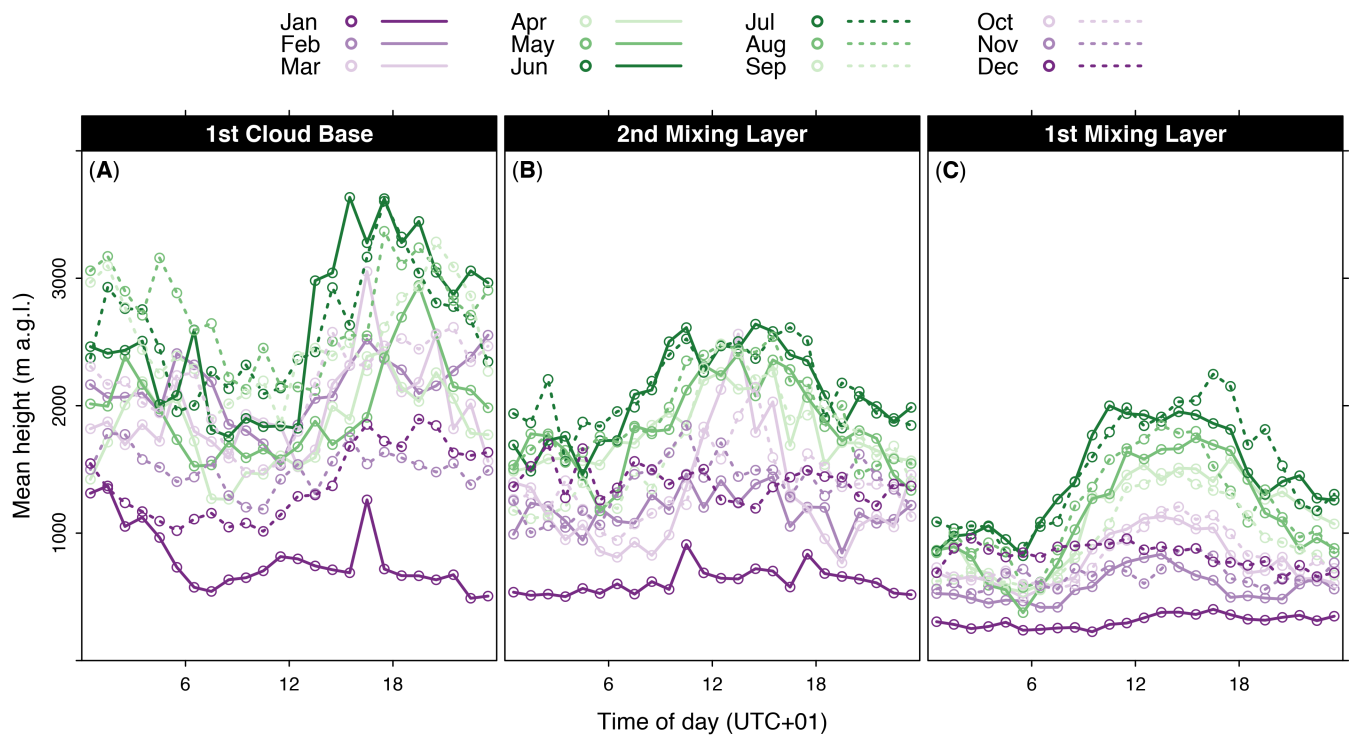


Figure S5. Shown are the monthly mean hourly height above ground (a.g.l.) of (A) the lowest cloud base, the (B) the second lowest mixing layer and (C) the lowest mixing layer as identified from ceilometer observations in the City Centre of Stuttgart, Germany. The observation period is 18 Jan 2017 to 31 Dec 2017.

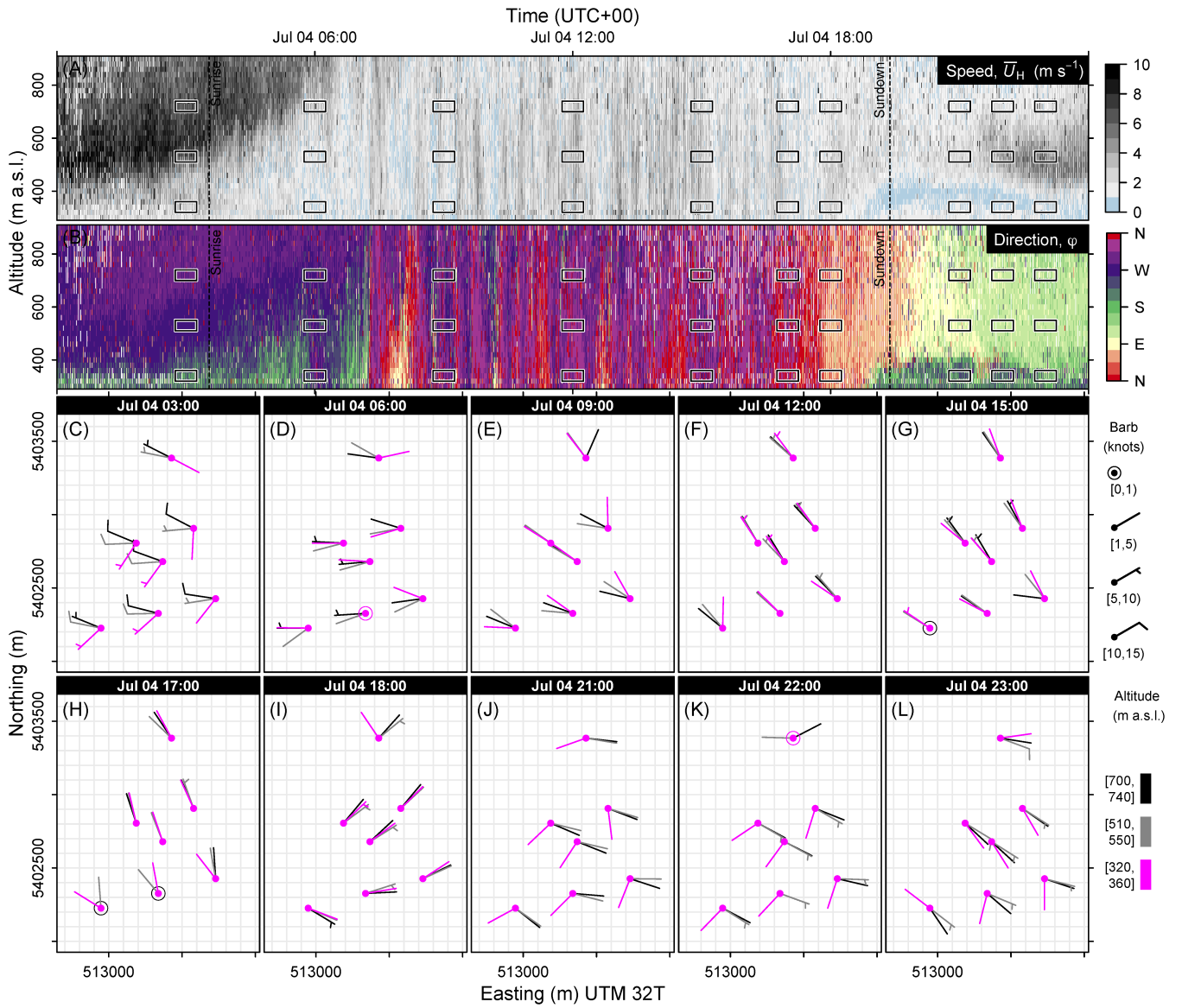


Figure S6. For a selected weak-wind day in summer (04 Jul 2017), a composite of the vertical profiles in Stuttgart City Centre of (A) the wind direction and (B) the wind speed are shown together with (C)(D)(E)(F)(G)(H)(I)(J)(K)(L) the mean wind field for selected locations, altitudes and periods in an area corresponding to Figure 1D. The altitudes and periods are annotated in panels (A) and (B) by black rectangles.

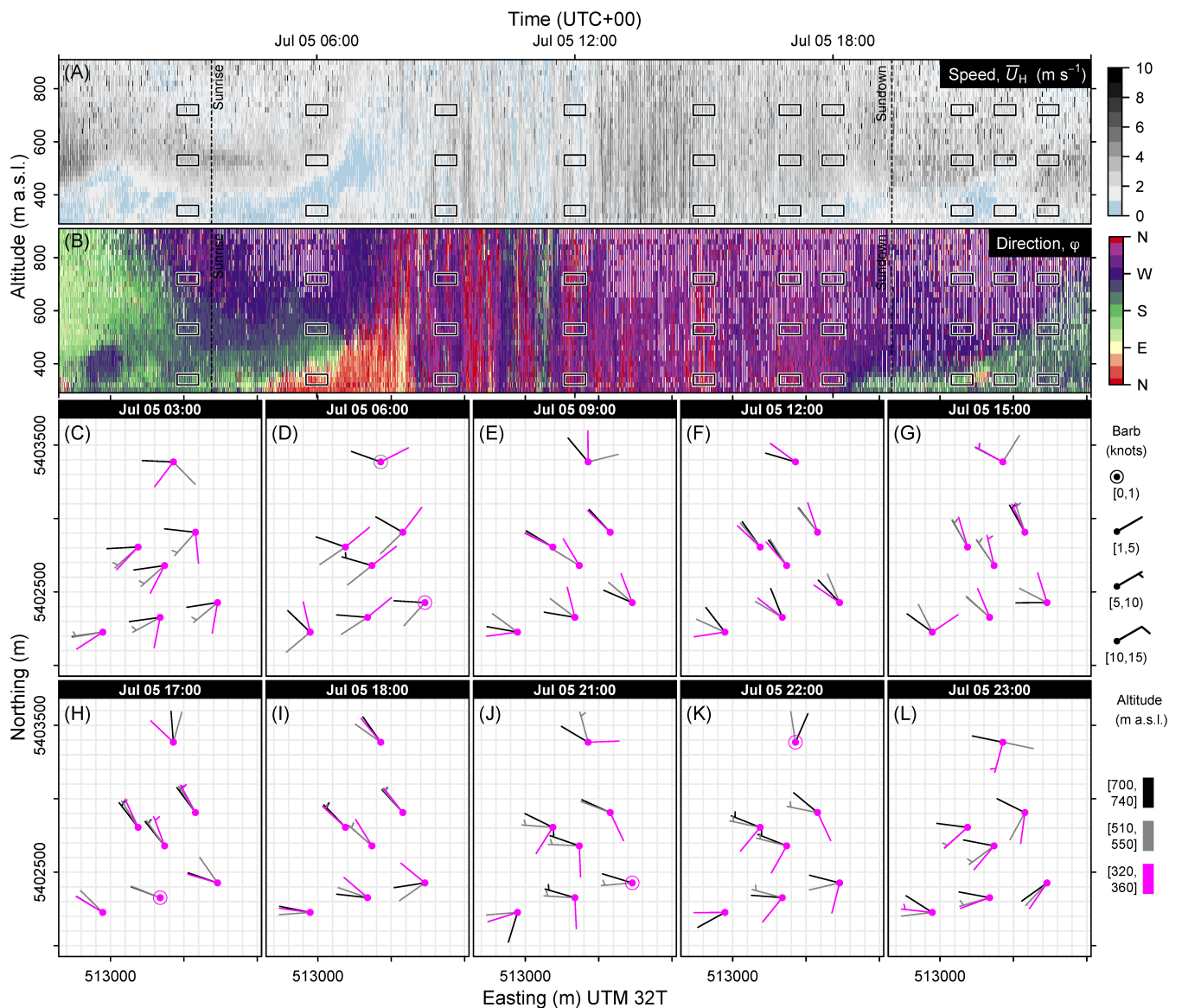


Figure S7. For a selected weak-wind day in summer (05 Jul 2017), a composite of the vertical profiles in Stuttgart City Centre of (A) the wind direction and (B) the wind speed are shown together with (C)(D)(E)(F)(G)(H)(I)(J)(K)(L) the mean wind field for selected locations, altitudes and periods in an area corresponding to Figure 1D. The altitudes and periods are annotated in panels (A) and (B) by black rectangles.

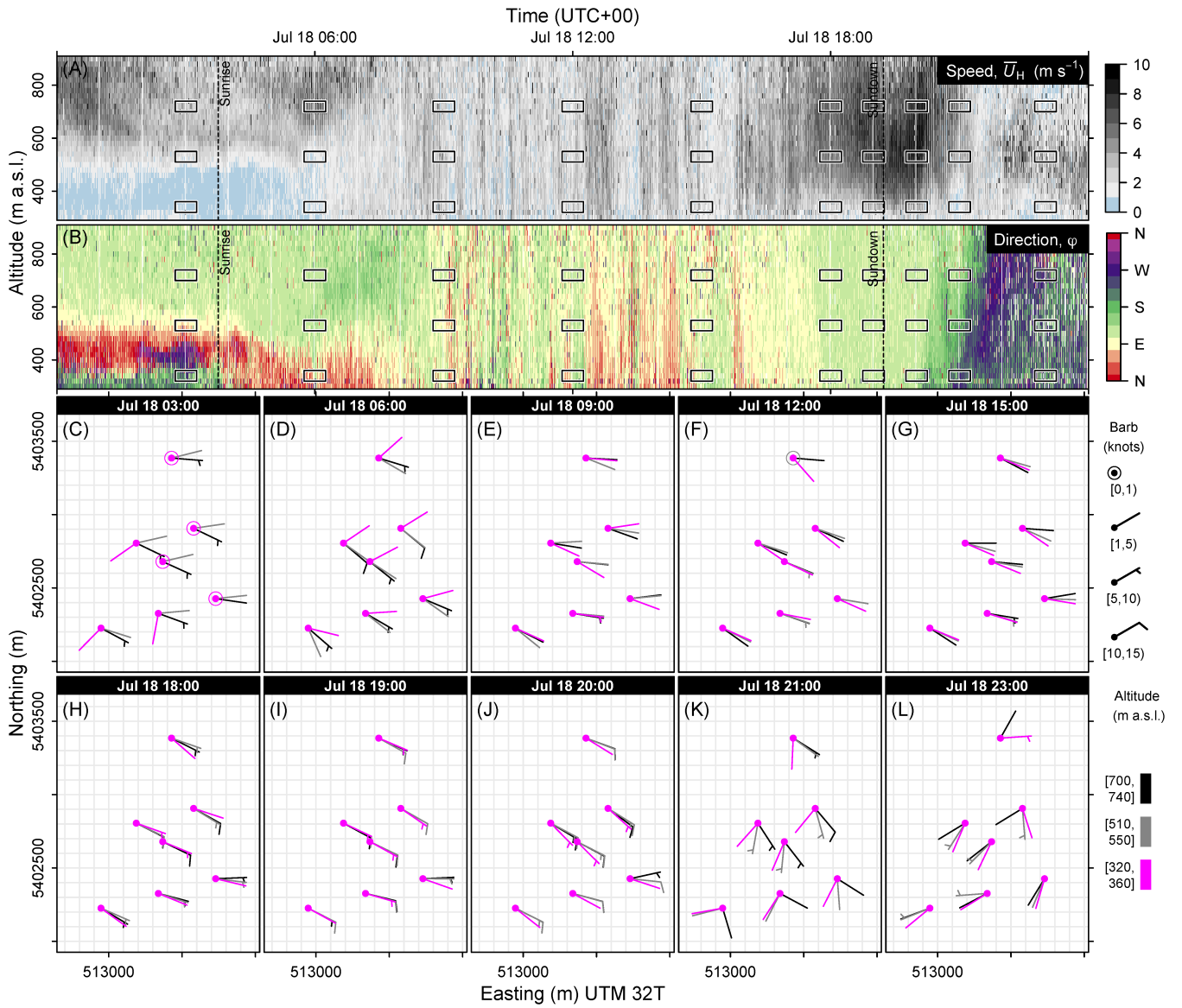


Figure S8. For a selected weak-wind day in summer (18 Jul 2017), a composite of the vertical profiles in Stuttgart City Centre of (A) the wind direction and (B) the wind speed are shown together with (C)(D)(E)(F)(G)(H)(I)(J)(K)(L) the mean wind field for selected locations, altitudes and periods in an area corresponding to Figure 1D. The altitudes and periods are annotated in panels (A) and (B) by black rectangles.

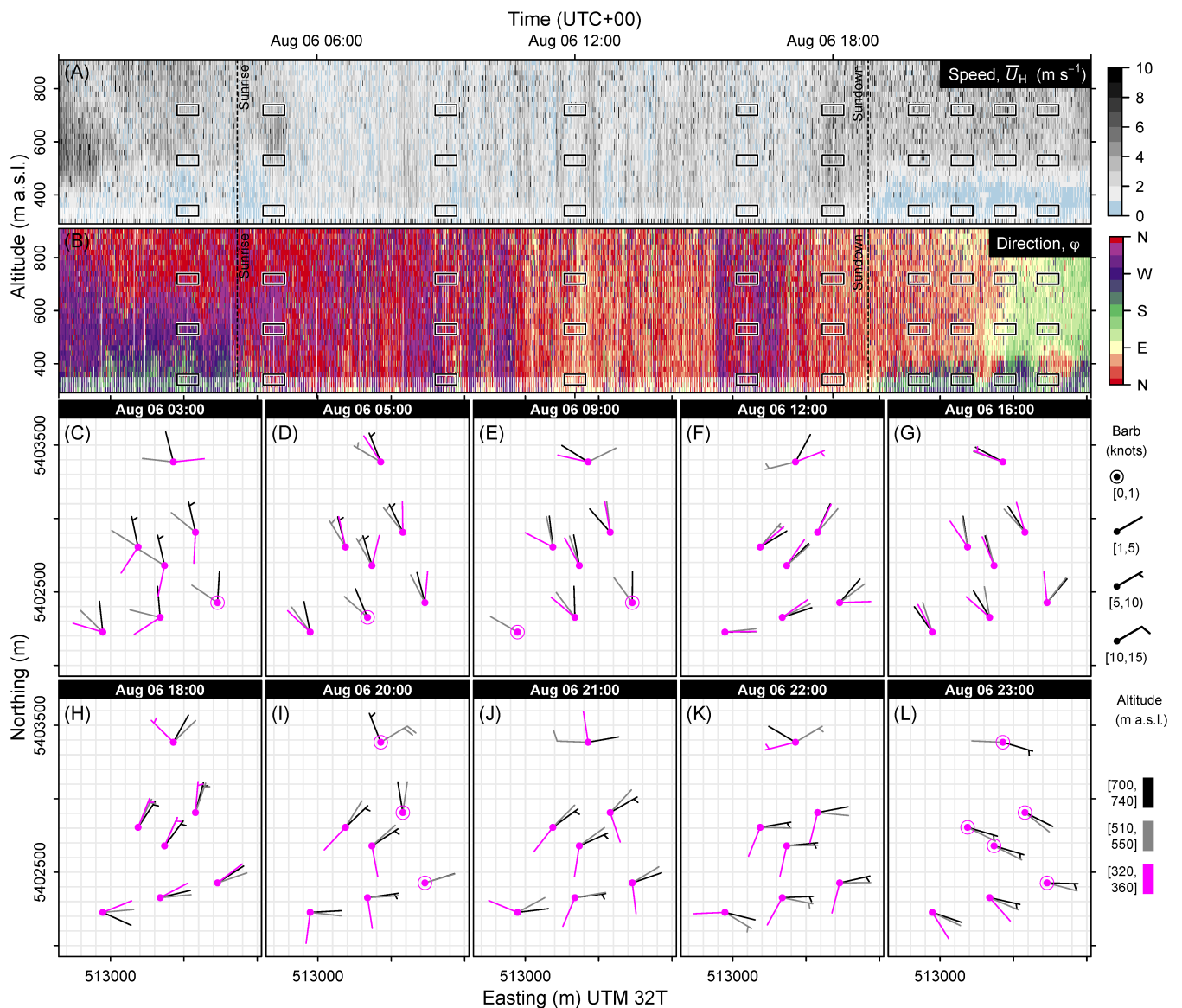


Figure S9. For a selected weak-wind day in summer (08 Aug 2017), a composite of the vertical profiles in Stuttgart City Centre of (A) the wind direction and (B) the wind speed are shown together with (C)(D)(E)(F)(G)(H)(I)(J)(K)(L) the mean wind field for selected locations, altitudes and periods in an area corresponding to Figure 1D. The altitudes and periods are annotated in panels (A) and (B) by black rectangles.

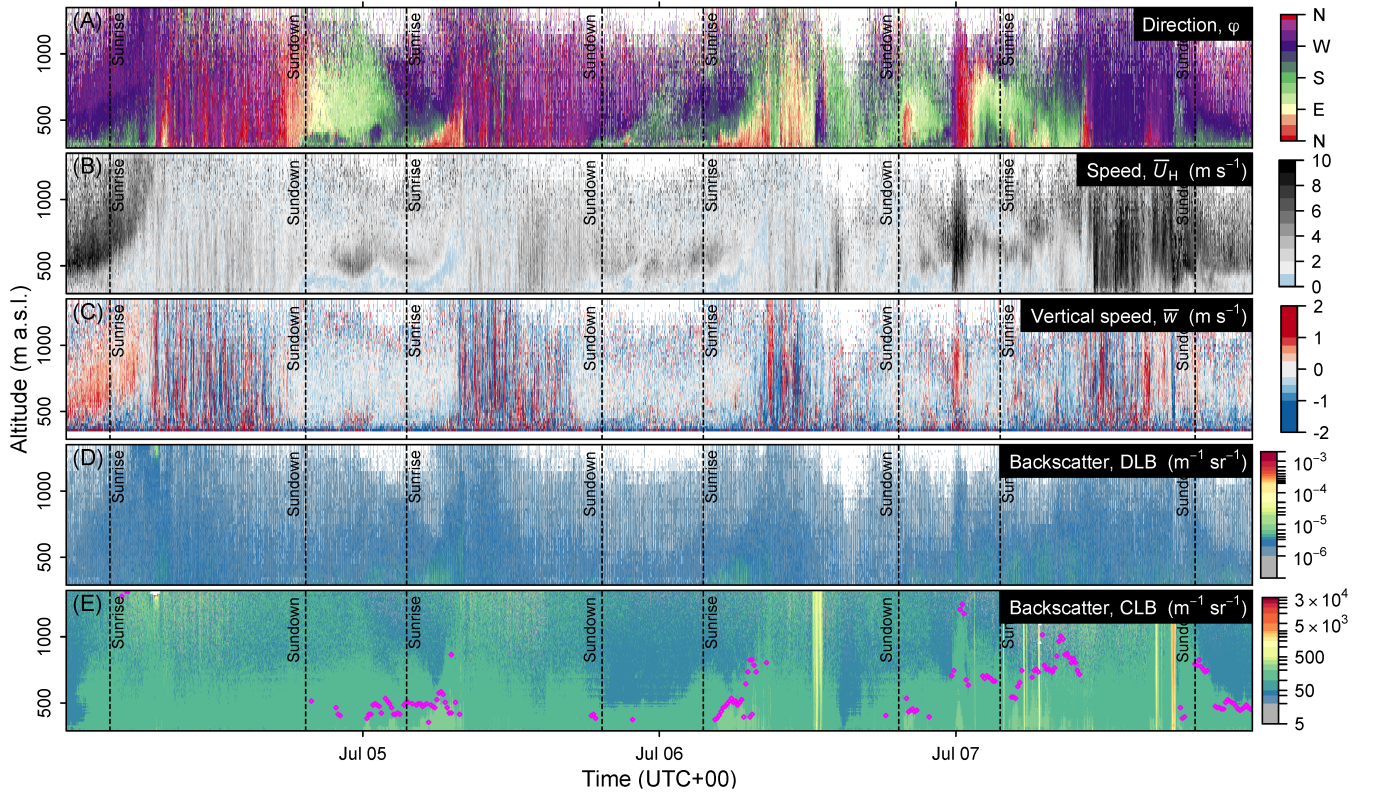


Figure S10. Vertical profiles of (A) wind direction (φ), (B) horizontal wind speed (\bar{U}_H), (C) vertical wind speed (w), (D) Doppler lidar backscatter (DLB) and (E) ceilometer back scatter (CLB) are shown for Stuttgart City Centre and period 04 Jul 2017 to 07 Jul 2017. The ceilometer-derived cloud base height and mixing layer height are shown in the bottom panel as white triangles and magenta diamonds, respectively.

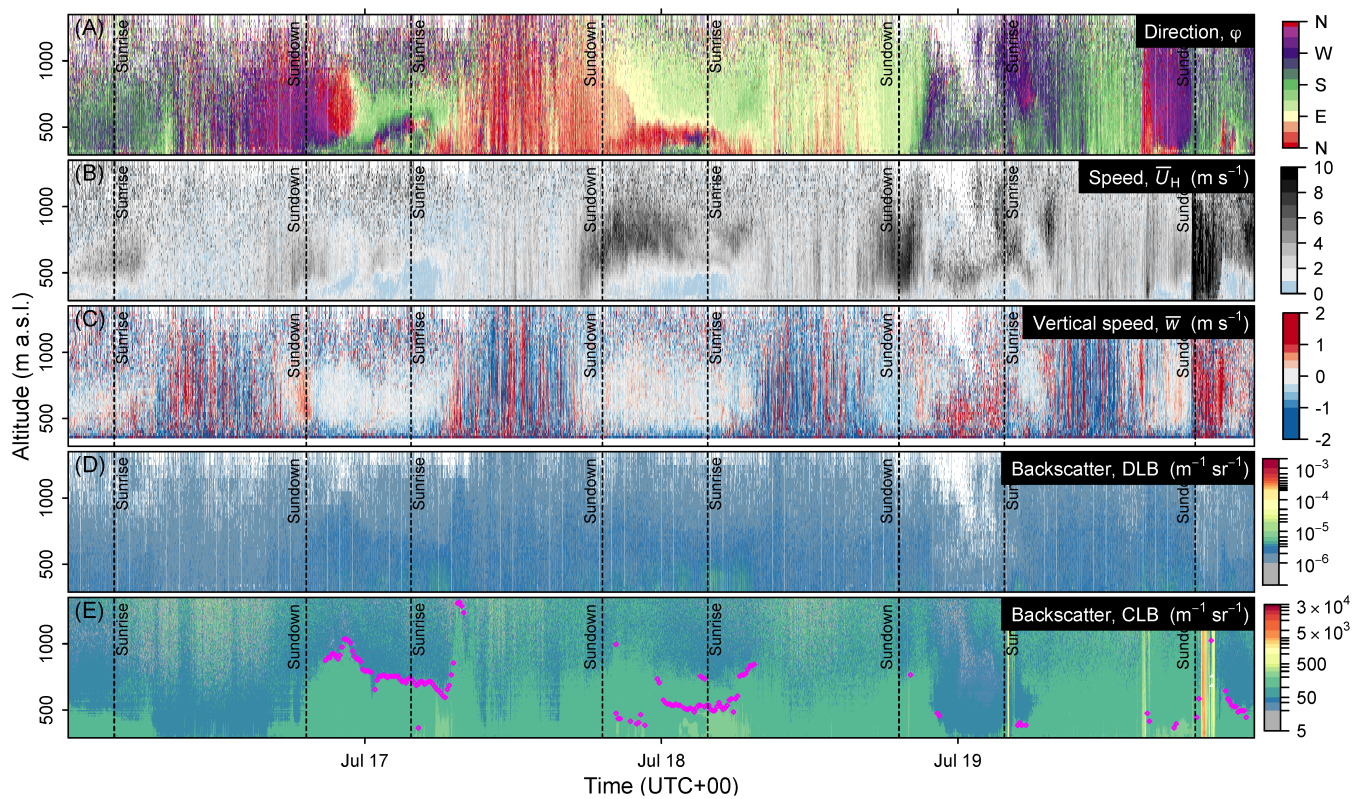


Figure S11. Vertical profiles of (A) wind direction (φ), (B) horizontal wind speed (\bar{U}_H), (C) vertical wind speed (w), (D) Doppler lidar backscatter (DLB) and (E) ceilometer back scatter (CLB) are shown for Stuttgart City Centre and period 16 Jul 2017 to 19 Jul 2017. The ceilometer-derived cloud base height and mixing layer height are shown in the bottom panel as white triangles and magenta diamonds, respectively.

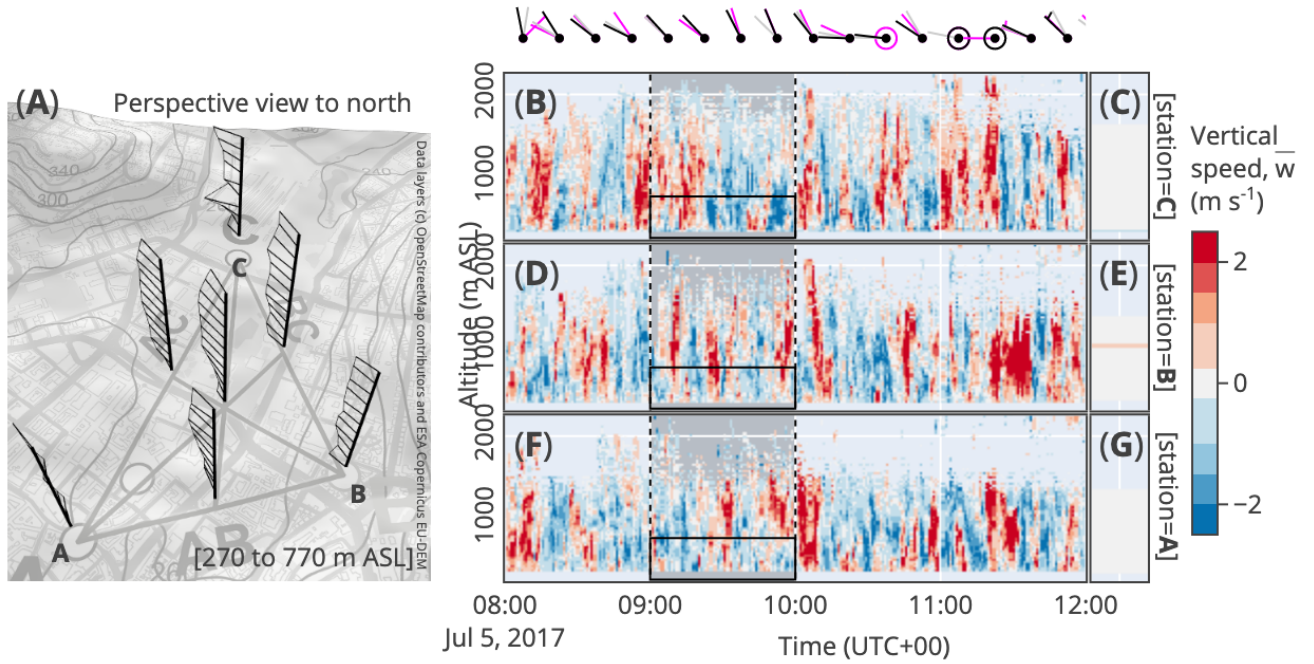


Figure S12. Shown for locations in Stuttgart City Centre are (A) the mean wind profiles for the highlighted period and altitude range in the right panels in a perspective view with a topography background, and (B)(D)(F) the vertical wind speed against time and altitude above DL station locations “A”, “B” and “C”, and (C)(E)(G) the mean vertical wind speed against altitude for the period between 08:00 to 10:00 UTC on 05 Jul 2017. Wind barbs shown on top represent the 15-min mean direction at 340 m, 530 and 720 m a.s.l., in magenta, grey and black, respectively.

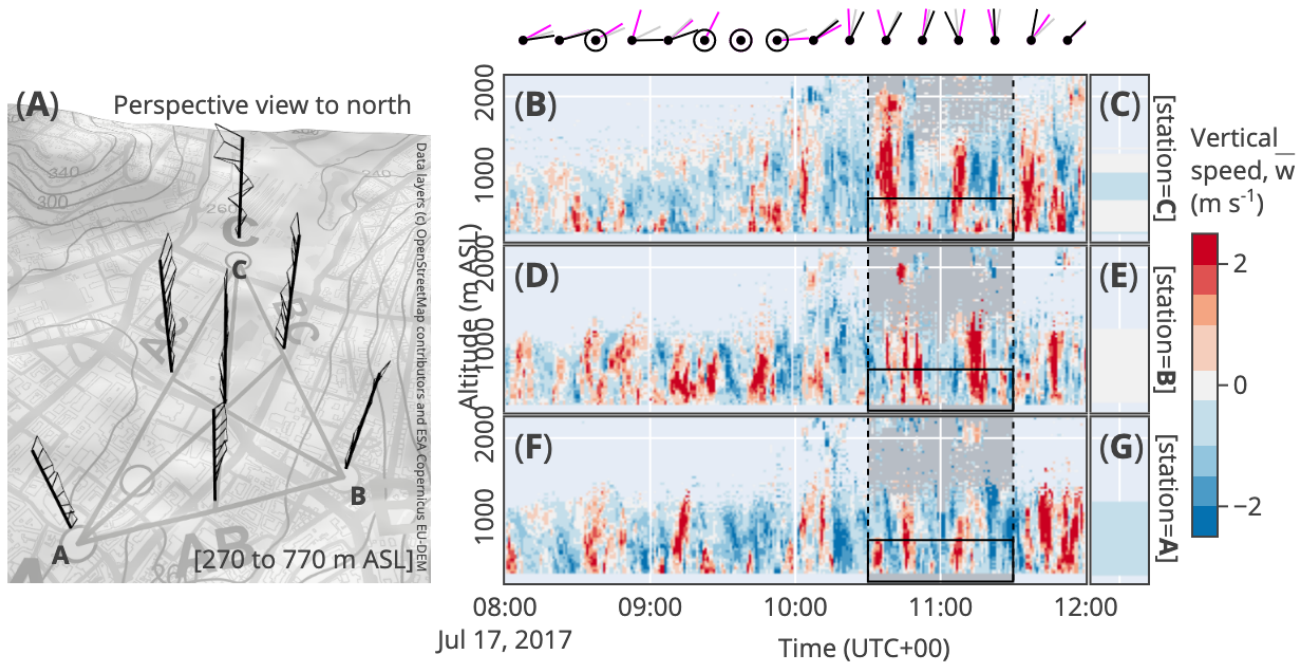


Figure S13. Shown for locations in Stuttgart City Centre are (A) the mean wind profiles for the highlighted period and altitude range in the right panels in a perspective view with a topography background, and (B)(D)(F) the vertical wind speed against time and altitude above DL station locations “A”, “B” and “C”, and (C)(E)(G) the mean vertical wind speed against altitude for the period between 10:30 to 11:30 UTC on 17 Jul 2017. Wind barbs shown on top represent the 15-min mean direction at 340 m, 530 m and 720 m a.s.l., in magenta, grey and black, respectively.

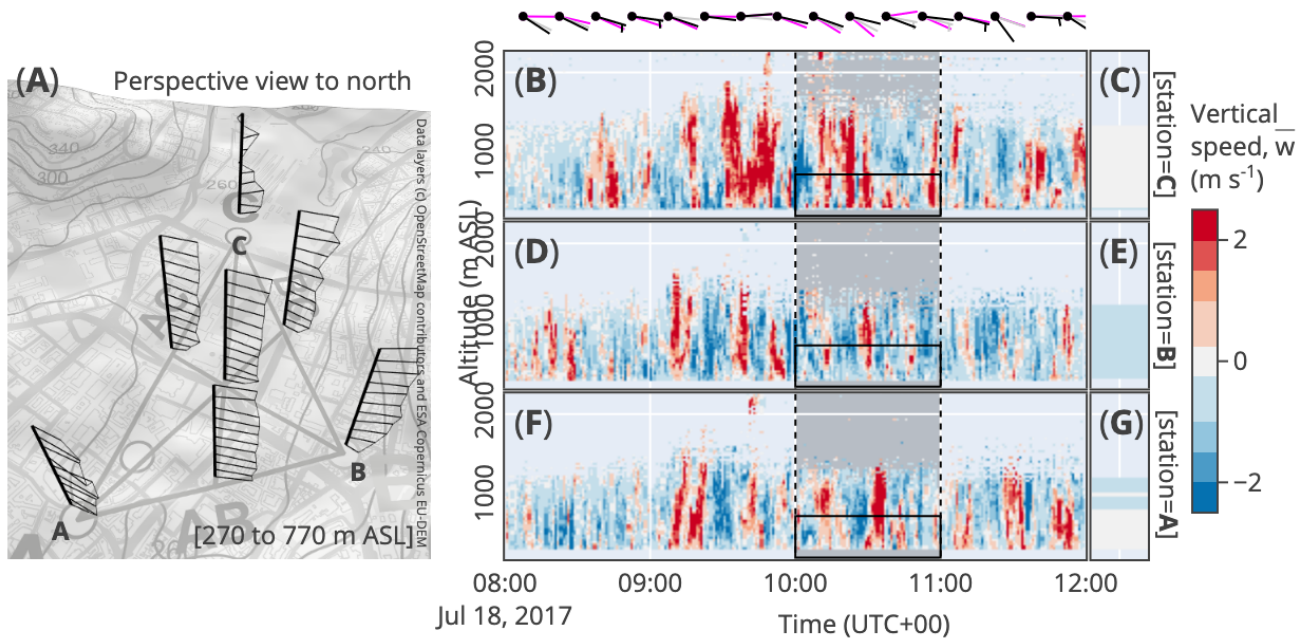


Figure S14. Shown for locations in Stuttgart City Centre are (A) the mean wind profiles for the highlighted period and altitude range in the right panels in a perspective view with a topography background, and (B)(D)(F) the vertical wind speed against time and altitude above DL station locations “A”, “B” and “C”, and (C)(E)(G) the mean vertical wind speed against altitude for the period between 10:00 to 11:00 UTC on 18 Jul 2017. Wind barbs shown on top represent the 15-min mean direction at 340 m, 530 m and 720 m a.s.l., in magenta, grey and black, respectively.

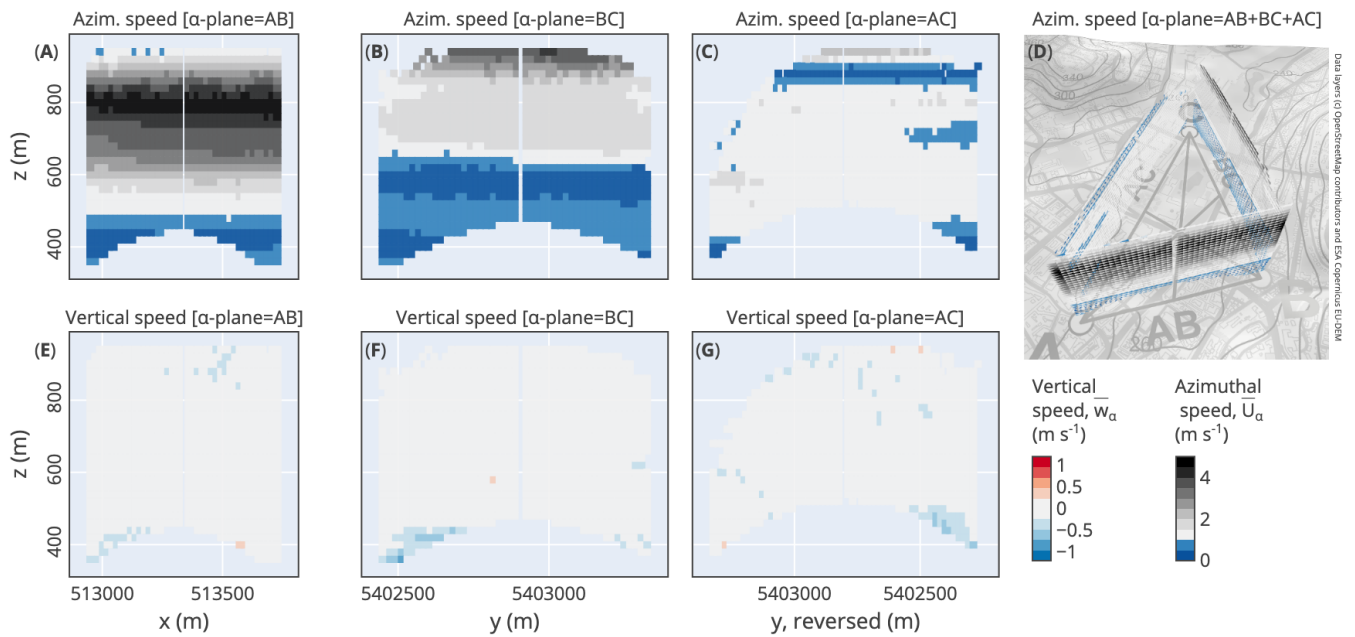


Figure S15. For the elevation planes between the three Doppler lidar locations in Stuttgart City Centre are shown the (A)(B)(C)(D) mean azimuthal speed and (E)(F)(G) the mean vertical speed against easting (x) or northing (y) and altitude a.s.l. (z), for 16:45 to 17:15 UTC on 14 Feb 2017.

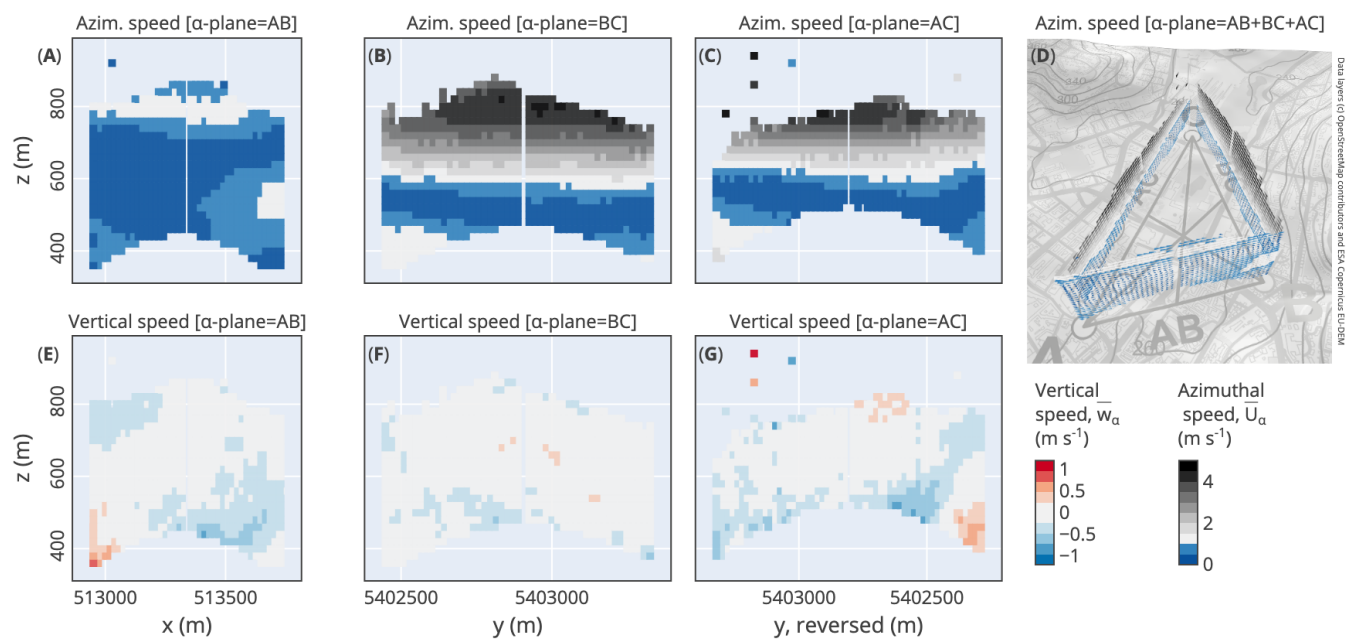


Figure S16. For the elevation planes between the three Doppler lidar locations in Stuttgart City Centre are shown the (A)(B)(C)(D) azimuthal speed and (E)(F)(G) the vertical speed against easting (x) or northing (y) and altitude a.s.l. (z), for 11:00 to 11:30 UTC on 14 Feb 2017.

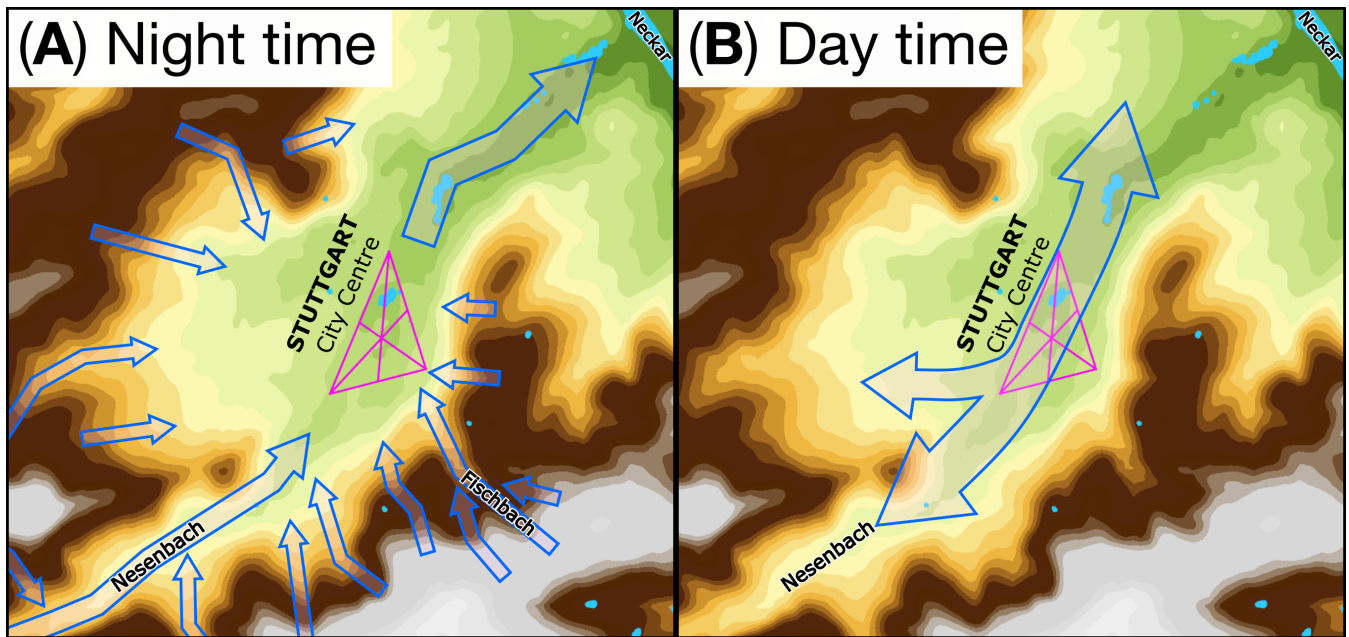


Figure S17. Conceptual diagram of competing flow regimes near the roof level during weak wind conditions in Stuttgart City Centre for (A) night-time drainage flow and (B) orographically channelled flow during the day. The flow is marked by open blue arrows on top of the topography color gradient and set up in magenta as shown in Figure 1.

REFERENCES

- Daniels, M. H., Lundquist, K. A., Mirocha, J. D., Wiersema, D. J., and Chow, F. K. (2016). A new vertical grid nesting capability in the weather research and forecasting (WRF) model. *Monthly Weather Review* 144, 3725–3747. doi:10.1175/mwr-d-16-0049.1
- Deardorff, J. W. (1980). Stratocumulus-capped mixed layers derived from a three-dimensional model. *Boundary-Layer Meteorology* 18, 495–527. doi:10.1007/BF00119502
- Dudhia, J. (1988). Numerical Study of Convection Observed during the Winter Monsoon Experiment Using a Mesoscale Two-Dimensional Model. *Journal of the Atmospheric Sciences* 46, 3077–3107. doi:10.1175/1520-0469(1989)046<3077:NSOCOD>2.0.CO;2
- Hong, S.-Y., Dudhia, J., and Chen, S.-H. (2004). A Revised Approach to Ice Microphysical Processes for the Bulk Parameterization of Clouds and Precipitation. *Monthly Weather Review* 132, 103–120. doi:10.1175/1520-0493(2004)132<0103:ARATIM>2.0.CO;2
- Hong, S.-Y., Noh, Y., and Dudhia, J. (2006). A New Vertical Diffusion Package with an Explicit Treatment of Entrainment Processes. *Monthly Weather Review* 134, 2318–2341. doi:10.1175/MWR3199.1
- Jiménez, P. A., Dudhia, J., González-Rouco, J. F., Navarro, J., Montávez, J. P., and García-Bustamante, E. (2011). A Revised Scheme for the WRF Surface Layer Formulation. *Monthly Weather Review* 140, 898–918. doi:10.1175/MWR-D-11-00056.1
- MLawer, E. J., Taubman, S. J., Brown, P. D., Iacono, M. J., and Clough, S. A. (1997). Radiative transfer for inhomogeneous atmospheres: RRTM, a validated correlated-k model for the longwave. *Journal of Geophysical Research* 102, 16663–16682. doi:10.1029/97JD00237
- Niu, G.-Y., Yang, Z.-L., Mitchell, K. E., Chen, F., Ek, M. B., Barlage, M., et al. (2011). The community Noah land surface model with multiparameterization options (Noah-MP): 1. Model description and evaluation with local-scale measurements. *Journal of Geophysical Research* 116, D12109. doi:10.1029/2010JD015139
- Pineda, N., Jorba, O., Jorge, J., and Baldasano, J. M. (2004). Using NOAA AVHRR and SPOT VGT data to estimate surface parameters: application to a mesoscale meteorological model. *International Journal of Remote Sensing* 25, 129–143. doi:10.1080/0143116031000115201
- Schmugge, T. J., Abrams, M. J., Kahle, A. B., Yamaguchi, Y., and Fujisada, H. (2003). Advanced Spaceborne Thermal Emission and Reflection Radiometer (ASTER). In *Remote Sensing for Agriculture, Ecosystems, and Hydrology IV*, eds. M. Owe, G. D’Urso, and L. Toullos. International Society for Optics and Photonics (SPIE), vol. 4879, 1 – 12. doi:10.1117/12.469693
- Talbot, C., Bou-Zeid, E., and Smith, J. (2012). Nested mesoscale large-eddy simulations with WRF: Performance in real test cases. *Journal of Hydrometeorology* 13, 1421–1441. doi:10.1175/jhm-d-11-048.1